

Spatial enhancement of elevation data using a single multispectral image

Mark J. Carlotto,* MEMBER SPIE
Pacific-Sierra Research Corporation
1400 Key Blvd., Suite 700
Arlington, Virginia 22209

Abstract. A new method for enhancing the spatial resolution of low-resolution digital elevation models (DEMs) using a single higher-resolution multispectral image is described. The method uses a nonlinear estimation algorithm to determine an empirical relationship between the spectral response of a pixel and the gradient or slope of its underlying elevation surface. This relationship is, in effect, the inverse of the reflectance map used in shape-from-shading to recover surface orientation from image brightness. However, unlike most shape-from-shading techniques, we do not assume constant albedo, nor do we assume a particular functional form for the reflectance map. A depth-from-gradient algorithm is used to generate high-resolution elevations from high-resolution gradients using the low-resolution elevations as boundary values. Experimental results demonstrate the ability to generate enhanced resolution elevation maps from global 1-km DEMs and Landsat Thematic Mapper imagery. © 2000 Society of Photo-Optical Instrumentation Engineers. [S0091-3286(00)02402-8]

Subject terms: shape from shading; image enhancement; nonlinear mean-square estimation; digital elevation models; multispectral imagery.

Paper 990087 received Mar. 1, 1999; revised manuscript received Aug. 3, 1999; accepted for publication Aug. 3, 1999.

1 Introduction

A variety of shape-from-shading (or photoclinometry) techniques for extracting elevations from remotely sensed data have been developed.¹⁻³ Most techniques assume that the albedo is constant and the reflectance map is known. Although the albedo can be treated as a constant in many planetary imaging situations and in some terrestrial cases, the albedo is almost always not constant and must be estimated on a pixel-by-pixel basis over the image. Eliason et al.⁴ describe a method based on clustering multispectral imagery using band ratios. Within each cluster the average brightness in a spectral band is used as an estimate of the albedo. By dividing the pixels within each cluster by the estimated albedo for that cluster, the variation in brightness due to the topography can be estimated and integrated to form an elevation surface. The success of the method depends critically on the clustering of band ratios, which are themselves sensitive to noise and to additive terms such as those caused by atmospheric scattering. Other approaches have been developed for estimating albedo locally from gray-scale imagery that make certain assumptions about the distribution of local surface normals.^{5,6}

Shape-from-shading techniques generally assume a particular functional form for the reflectance map.⁷ The Lambertian model is often used because of its simplicity. However, many surface materials, particularly those that are man-made, are not Lambertian.

Previously we demonstrated the ability to estimate the topographic component of brightness from multispectral

imagery.⁸ Building on this work, a method is described for spatially enhancing low-resolution elevation data using a single higher-resolution multispectral image. Instead of an explicit reflectance function, a nonlinear estimator is used to determine an optimal mapping between spectral values in a multispectral image and the gradients of a coregistered low-resolution digital elevation model (DEM). This mapping, which is represented as a lookup table, assigns to each unique combination of spectral values that occur in the image their x - and y -gradient values estimated from the low-resolution DEM. Because the gradient estimates are computed over higher-resolution pixels, they are higher in resolution than the original gradients. Elevation sharpening is accomplished by integrating these estimated gradients into a higher-resolution elevation surface using the existing low-resolution elevations as boundary values.

Since image brightness is a function of the derivatives of the elevation surface, shape-from-shading techniques have difficulty in recovering low-frequency elevation data in the presence of noise. As a result, hybrid methods have been developed that combine shape-from-shading with information from other sources such as stereo⁹ and low-resolution terrain data.¹⁰ Our method, like that developed by Frankot and Chellappa, uses lower-resolution terrain data. An important difference between these two methods is that ours does not assume a particular functional form for the reflectance map, nor does it assume the albedo is constant across the scene.

2 Shape from Shading

The majority of shape-from-shading algorithms assume the albedo within a scene is constant (surface material compo-

*Address all correspondence to 5 Ryan Place, Beverly MA 01915 (markc@psrw.com).

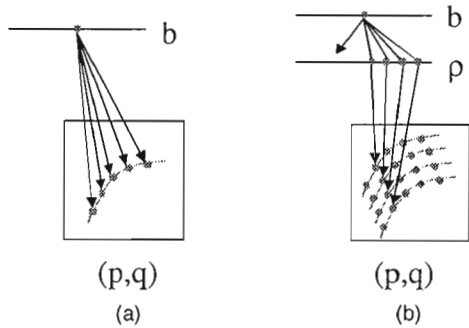


Fig. 1 Surface gradients cannot be recovered directly from image brightness. For constant albedo and a Lambertian surface the gradients corresponding to a given brightness value lie along a conic section (a). Not knowing the albedo further complicates the situation (b).

sition or land cover is homogeneous), so that image irradiance (brightness) can be related directly to surface reflectance:

$$b(i,j) \propto R[p(i,j),q(i,j)], \quad (1)$$

where R is the reflectance map and $p(i,j)$ and $q(i,j)$ are the two components of the surface gradient (slope). In most practical applications the surface material composition varies over the scene. The image brightness thus depends on the albedo of the surface material as well as on its reflectance:

$$b(i,j) \propto \rho(i,j)R[p(i,j),q(i,j)]. \quad (2)$$

However, even when the albedo is constant, surface gradients cannot be uniquely determined from image brightness without additional constraints; e.g., for a Lambertian surface, the gradients corresponding to a given brightness value lie along conic sections. Unknown albedo further

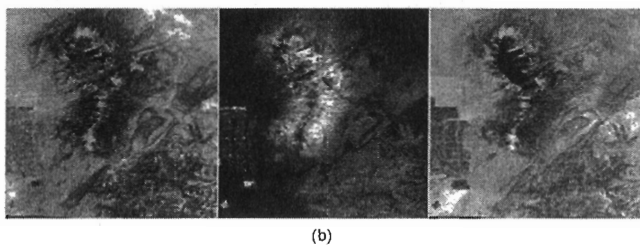
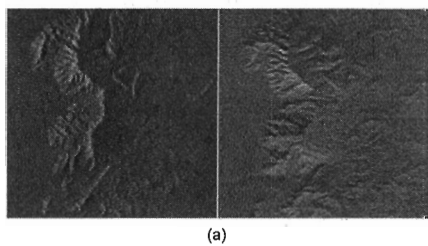


Fig. 2 (a) Gradients in horizontal (left) and vertical (right) directions, computed from DEM; (b) Ratio images for selected band ratios (from left to right 3/2, 4/3, and 5/4) of coregistered Landsat TM image.

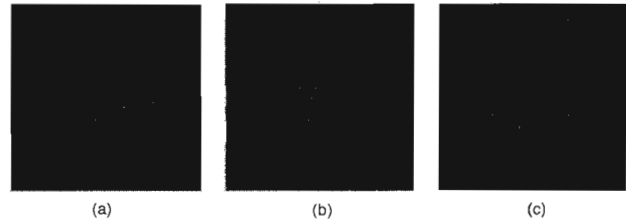


Fig. 3 Ratio images plotted as a function of the x and y components of the gradient (horizontal and vertical axes): (a) band 3/2 ratio, (b) Band 4/3 ratio, (c) Band 5/4 ratio.

complicates shape-from-shading, since a given brightness value can correspond to many more possible gradients (Fig. 1).

For multispectral data the brightness is the n th spectral band

$$b(i,j,n) \propto \rho(i,j,n)R[p(i,j),q(i,j)], \quad (3)$$

where $\rho(i,j,n)$ is the spectral albedo. It is usually assumed that the reflectance map does not depend on wavelength.

Shape-from-shading algorithms tacitly assume that albedo and surface gradients are unrelated to one other. However, it is often observed that vegetation type, state, and density vary with the topography, and that land use is often constrained by the topography. Figures 2 and 3 illustrate this point. Figure 2(a) shows the two components of the gradient computed from a 25-m DEM over a study area in northern New Mexico. Assuming the reflectance map does not depend on wavelength [Eq. (3)], the ratio of spectral albedos can be computed on a pixel-by-pixel basis by dividing one spectral band by another (provided the path radiance has been removed). Figure 2(b) shows three ratio images derived from a Landsat Thematic Mapper[†] (TM) image registered to the DEM. To visualize the relation between spectral albedo and slope we plot the band-ratio image values as a function of the x and y components of their corresponding slope values computed from the coregistered DEM (Fig. 3). When there is no relation between spectral albedo and slope (i.e., between land cover and topography), the distributions of band ratio values are uniform. In Figs. 3(a) and 3(b) the band 3/2 and 4/3 ratios have an anisotropic distribution as a function of slope aspect. In Fig. 3(c) the band 5/4 ratio varies radially as a function of slope angle. Over this area the northern and eastern slopes of the Sandia Mountains are vegetated, while the southern and western slopes are not. There are also many subtle differences within slope regimes. The distributions in Fig. 3 suggest that, for this scene, there does appear to be a relation between the spectral albedo and slope.

As noted earlier, variable albedo is usually thought to complicate shape-from-shading. But if the variation in spectral albedo is related to slope, can this relationship be used to simplify the shape-from-shading problem? Combining the relations between slope and reflectance (reflectance map) and between slope and albedo into a single function, we can rewrite Eq. (3) as

[†]Landsat TM has seven spectral bands. Bands 1 to 3 are in the visible; bands 4, 5, and 7 are reflective infrared (IR), and band 6 is a thermal band. We use bands 1 to 5 and 7, which have a spatial resolution of 25 m/pixel.

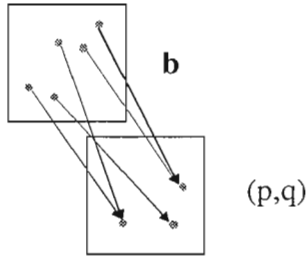


Fig. 4 Relation between spectral and gradient spaces for the inverse mapping in Eq. (5) to exist.

$$[b(i,j,1), b(i,j,2), \dots, b(i,j,N)] = F[p(i,j), q(i,j)], \quad (4)$$

which gives the spectral response of a pixel as a function of its slope. For this function to exist we require that each surface gradient be associated with one and only one spectral value. In order to determine the two components of the gradient of a pixel from its spectral response, we need to invert Eq. (4):

$$[p(i,j), q(i,j)] = F^{-1}[b(i,j,1), b(i,j,2), \dots, b(i,j,N)]. \quad (5)$$

But for F to be invertible, the relationship between spectral and gradient spaces must be one-to-one; i.e., each spectral value can be associated with one and only one surface gradient value, and vice versa.

Instead of attempting to model and invert the function in Eq. (4) (which is unknown), we use a nonlinear mean-square estimation approach to determine the inverse mapping [Eq. (5)] directly. For this mapping to exist we require that each spectral value be associated with one and only one surface gradient, but allow multiple spectral values to have the same gradient (Fig. 4).

3 Nonlinear Estimation

We first reduce the dimensionality of the spectral data using the principal components (PC) transformation $\mathbf{u} = \mathbf{A}\mathbf{b}$ to map the original spectral vector $\mathbf{b} = [b(1), b(2), \dots, b(N)]$ into a lower-dimensional vector $\mathbf{u} = [u(1), u(2), \dots, u(N')]$. This is done for two reasons. First, the intrinsic dimensionality of the spectral data is lower than the actual number of bands (for TM it is typically between 2 and 3). The PC transform effectively reduces the dimensionality of the data without a significant loss of information. Second, the current software algorithm is limited to no more than three dimensions ($N' \leq 3$).

We wish to compute functions relating \mathbf{u} to the x and y components of the gradient:

$$p = f_p[\mathbf{u}], \quad (6)$$

$$q = f_q[\mathbf{u}].$$

Instead of attempting to develop an analytic model, we use *training data* to determine these functions empirically.

Let $v = f(u)$ be a unknown nonlinear function relating the two random variables, u and v , and let $p(u, v)$ be their

joint density. The function we seek minimizes the expected value of the squared error between v and its estimate $\bar{v} = f(u)$:

$$E[v - f(u)]^2 = \int_{-\infty}^{\infty} \int_{-\infty}^{\infty} [v - f(u)]^2 p(u, v) du dv \quad (7)$$

and is given by the conditional mean¹¹

$$f(u) = E[v|u] = \int_{-\infty}^{\infty} v p(v|u) dv, \quad (8)$$

where the conditional density $p(v|u) = p(u, v)/p(u)$.

For elevation sharpening we use the gradients computed from a registered low-resolution DEM together with higher-resolution multispectral imagery as training data. The optimal (in the minimum-mean-squared-error sense) estimate of the slope as a function of the spectral response is given by

$$\bar{v} = f(\mathbf{u}) = \sum_v v p(v|\mathbf{u}) = \sum_v v p(v, \mathbf{u}) / \sum_v p(v, \mathbf{u}), \quad (9)$$

where \mathbf{u} is the transformed spectral data and v is either component of the gradient. As the number of dimensions increases, representing the joint density with an $(N' + 1)$ -dimensional array becomes increasingly inefficient. We thus implement the nonlinear estimator with hash tables expressing Eq. (9) in a different but equivalent form:

$$f(\mathbf{u} = \mathbf{u}_m) = \frac{1}{N_m} \sum_{(i,j) \in S_m} v(i,j), \quad (10)$$

where S_m is the set of pixels in the image with the value $\mathbf{u}(i,j) = \mathbf{u}_m$, and N_m is the number of pixels in S_m . The number of entries in the table M is equal to the cardinality of \mathbf{u} (the number of unique vectors or combinations). To compute the m th entry we average v over those pixels where $\mathbf{u}(i,j) = \mathbf{u}_m$ and store that value in the table (see the pseudocode in Fig. 5). The tables for the x and y components of slope are thus

Create 2 hash tables, $f()$ and $g()$ each with at least M elements, and initialize to zero.

Compute lookup table:

```

For each pixel (i,j){
    m = HashCode[u(i,j,1), u(i,j,2), ... u(i,j,N')]
    If g(m) = 0 {
        g(m) = 1;
        f(m) = v(i,j);
    }
    Else {
        g(m) = g(m) + 1;
        f(m) = f(m) + v(i,j);
    }
}
For each hash code m
    f(m) = f(m)/g(m)
    
```

Use lookup table:

```

For each pixel (i,j){
    m = HashCode[u(i,j,1), u(i,j,2), ... u(i,j,N')]
    v-est(i,j) = f(m)
}
    
```

Fig. 5 Nonlinear mean-square estimation algorithm.

$$f_p(\mathbf{u}=\mathbf{u}_m) = \frac{1}{N_m} \sum_{(i,j) \in S_m} p_L(i,j),$$

$$f_q(\mathbf{u}=\mathbf{u}_m) = \frac{1}{N_m} \sum_{(i,j) \in S_m} q_L(i,j),$$
(11)

where p_L and q_L are the gradients derived from the lower-resolution DEM training data. High-resolution gradient images are then generated from the multispectral image by table lookup:

$$p_H(i,j) = f_p[\mathbf{u}(i,j)],$$

$$q_H(i,j) = f_q[\mathbf{u}(i,j)].$$
(12)

4 Elevation Sharpening Process

Estimating high-resolution gradients from the multispectral image is the key element of the elevation sharpening process. The overall process flow is depicted in Fig. 6. The inputs consist of the low-resolution DEM to be sharpened, registered to a higher-resolution multispectral image (25-m Landsat TM in the present discussion). The output is the sharpened DEM at the same pixel resolution as the multispectral image.

The DEM is first resampled to the same spatial resolution as the multispectral imagery with intermediate pixel values interpolated. The low-resolution gradients are then computed from the resampled low resolution DEM by

$$p_L(i,j) = \frac{1}{2\epsilon} z_L(i+1,j) - z_L(i-1,j),$$

$$q_L(i,j) = \frac{1}{2\epsilon} z_L(i,j+1) - z_L(i,j-1),$$
(13)

where ϵ is the pixel spacing.

Next the PC transform is used to reduce the dimensionality of the spectral data. The spectral covariance matrix was computed for TM bands 1 to 5 and 7 over the study area (Fig. 2), and the eigenvectors and eigenvalues determined. The eigenvalues were 1939.46, 217.40, 54.51, 24.04, 16.30, and 5.52. The eigenvectors corresponding to three largest eigenvalues were then used to compute the first three principal components. The number of unique spectral vectors (the number of entries in the hash tables) depends on the dimensionality of \mathbf{u} . For example, using

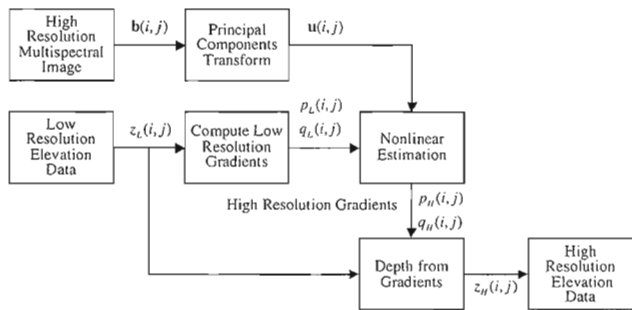


Fig. 6 Overview of elevation sharpening process.

only the first principal component, 188 unique combinations occur; using the first two principal components, 8250 unique combinations occur; using the first three principal components, 130,837 unique combinations occur. We use the first three principal components for the experiments in the next section.

The nonlinear estimator described in the previous section is then used to estimate the high-resolution gradients from the first three principal components of the Landsat TM image. This involves computing two lookup tables, one for each component of the gradient, from the coregistered principal component and low-resolution gradient images [Eq. (11)]. The tables are then used to generate high-resolution gradients from the principal-component images [Eq. (12)].

A depth-from-gradient algorithm¹² is used next to generate high-resolution elevations from the high-resolution gradients:

$$z_H^{t+1}(i,j) = \bar{z}_H^t(i,j) - \frac{\epsilon}{8} [p_H(i+1,j) - p_H(i-1,j) + q_H(i,j+1) - q_H(i,j-1)],$$
(14)

where

$$\bar{z}_H(i,j) = \frac{1}{4} [z_H(i+1,j) + z_H(i-1,j) + z_H(i,j+1) + z_H(i,j-1)].$$
(15)

At each iteration the algorithm locally averages the high-resolution elevations from the previous iteration and subtracts horizontal and vertical differences of the estimated high-resolution gradients. As is, the above algorithm provides only relative elevations. To obtain absolute elevations, at each iteration the estimate is forced to conform to the low-resolution elevation data at the original low-resolution sample points Z_L :

$$z_H^{t+1}(i,j) = \begin{cases} z_L(i,j), & (i,j) \in Z_L, \\ z_H^t(i,j) & \text{otherwise.} \end{cases}$$
(16)

For example, when sharpening a 1-km DEM to 25 m, the high-resolution estimate is replaced by a low-resolution elevation value every 40 pixels in the x and y directions.

5 Experimental Results

To illustrate the elevation sharpening process we return to the study area in northern New Mexico considered earlier. Figure 7 shows a 1024-by-1280-pixel, 25-m-elevation data

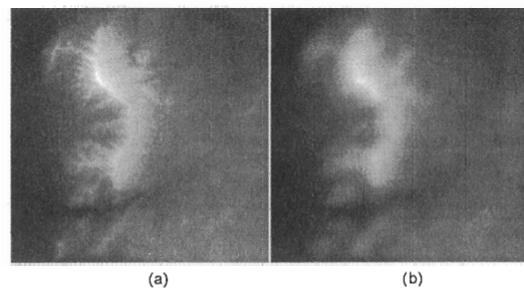


Fig. 7 USGS 25-m DEM (a) and simulated 1-km DEM (b).

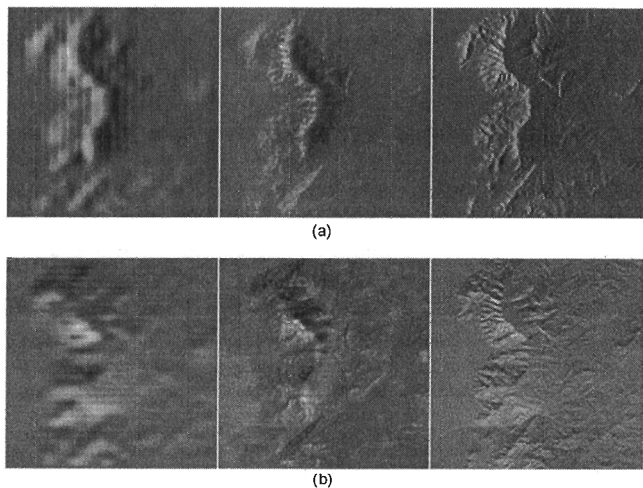


Fig. 8 Gradient images, (a) x-gradient and (b) y-gradient: 1-km (left), estimated 25-m (middle), and true 25-m (right).

image derived from a USGS DEM. The elevations range from 1533 to 3248 m over an area 25.6 by 31.25 km in size. The Sandia mountains run down the middle of the study area with the eastern portion of Albuquerque to the left. The area contains a diversity of land use and land cover types, including low- and high-density urban, grassland/agriculture, rangeland, deciduous and coniferous vegetation, water, and bare soil/rock.

Beside the 25-m elevation image is a simulated 1-km-resolution DEM produced by smoothing and subsampling the 25-m DEM. The goal of the elevation-sharpening experiment is to sharpen the 1-km DEM with the 25-m Landsat image shown earlier in Fig. 2 using the original 25-m DEM as ground truth for evaluation. The Landsat was acquired Apr. 15, 1994. The solar azimuth and zenith angles at the time of acquisition were 123 and 52 deg, respectively.

Figure 8 shows the low-resolution gradients derived from the simulated 1-km DEM, the gradients computed

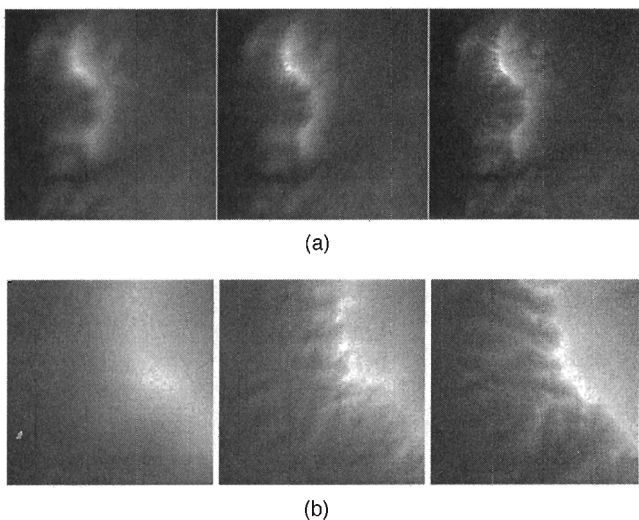


Fig. 9 Elevation-sharpening results, 1-km DEM (left), sharpened 1-km DEM (center), and original 25-m DEM (right): (a) over entire study area; (b) over a portion of the study area at full resolution.

Table 1 Mean and standard deviation of the vertical errors between actual and estimated 25-m DEMs for several interpolation schemes and for elevation sharpening.

Estimate	Mean (m)	Standard deviation (m)
Nearest neighbor	-0.35	48.7
Bilinear	-0.38	33.9
Cubic	0.19	30.8
Elevation sharpening	-0.06	29.5

from the 25-m Landsat image using the nonlinear estimation algorithm, and the true gradients of the original 25-m DEM. The gradient images have been scaled for display.

Elevation-sharpening results are presented in Fig. 9. The original 1-km, sharpened 1 km (estimated 25-m), and 25-m DEMs are shown in Fig. 9(a). A portion of the data at full resolution is shown in Fig. 9(b).

A significant increase in spatial detail is apparent in Fig. 9. But to what extent is elevation sharpening better than simple pixel interpolation? Assuming the DEM and multispectral image are accurately registered, the mean and standard deviation of the difference between the interpolated or sharpened 1-km and actual 25-m data (the vertical error) is one measure of accuracy. The results in Table 1 suggest that elevation sharpening is only slightly better than simply interpolating the DEM.

Sample transects (Fig. 10) indicate that the image and DEM are not accurately registered in some areas; i.e., estimated elevations are shifted horizontally relative to the true elevations. This leads to errors, particularly in high-slope areas. In order not to be penalized by misregistration, we consider a point to be accurate to a given horizontal accuracy if it lies within a region bounded by maximum and

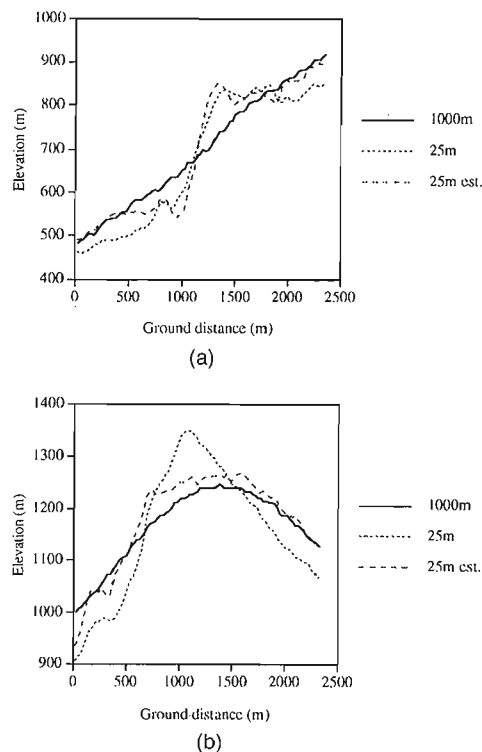


Fig. 10 Sample transects from a hillside (a) and at a peak (b).

Table 2 Fraction of interpolated and sharpened 1-km DEMs within a given horizontal error of the 25-m DEM.

Horizontal error (m)	Fraction of DEMs	
	Sharpened	Interpolated
0	0.15	0.16
25	0.34	0.25
50	0.48	0.34
75	0.58	0.49
100	0.67	0.52

Table 3 Comparison of gradient-image statistics.

DEM	Standard deviation	
	x gradients	y gradients
True 25-m	13.3	11.7
Sharpened 1-km	4.6	2.4

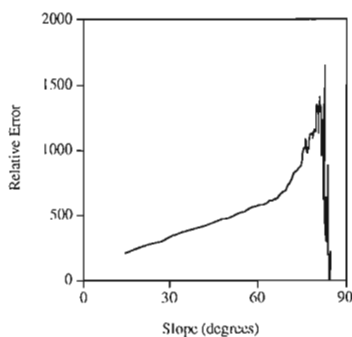


Fig. 11 Distribution of errors as a function of slope angle.

minimum elevations within a given distance from that point:

$$z^{+\epsilon}(i,j) > z_H(i,j) > z^{-\epsilon}(x,y), \tag{17}$$

where

$$z^{+\epsilon}(i,j) = \max_{k,l: k^2+l^2 < \epsilon_H^2} z(i+k,j+l),$$

$$z^{-\epsilon}(i,j) = \min_{k,l: k^2+l^2 < \epsilon_H^2} z(i+k,j+l), \tag{18}$$

and $z(x,y)$ and $z_H(x,y)$ are the true and estimated elevation surfaces. Table 2 gives the fraction of the cubic-interpolated and sharpened 1-km elevation images within a given horizontal distance of the true 25-m surface [i.e., the fraction of the estimate that satisfies Eq. (17) for a given horizontal error]. The results indicate that the sharpened 1-km estimate is a better approximation to the 25-m DEM for horizontal errors of 1 pixel (25 m) or more. The greatest improvement (14%) is at 50 m.

6 Discussion

Table 3 compares the standard deviations of the true and estimated 25-m gradient images. Because they were derived from a 1-km DEM, the estimated 25-m slopes are smaller in magnitude (slope angle) than the true 25-m slopes. It is also noted that since the sun is more closely aligned with the x axis, there is a greater amount of shading information in that direction in the image, and so the estimated x gradients have a greater dynamic range than the y gradients. One would therefore expect that elevation errors would be greater in high-slope areas and for slopes that are perpendicular to the solar direction.

Figure 11 plots the elevation error as a function of slope. The lower range of slopes noted above leads to elevation errors in high-slope areas.

The greatest amount of shading information is in the solar-antisolar direction. Figure 12 plots the distribution of elevation errors as a function of slope aspect (azimuth angle). As expected, the errors peak in the direction of the western slopes of the Sandia mountains (the highest-slope areas are on the western side of the Sandia mountains) and in directions perpendicular to the solar-antisolar line.

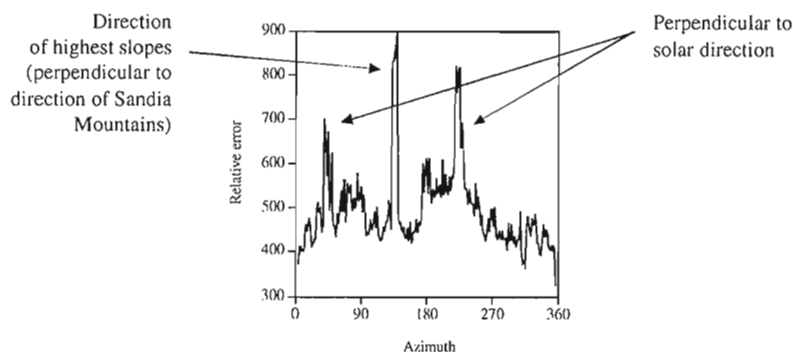


Fig. 12 Distribution of errors as a function of slope aspect.

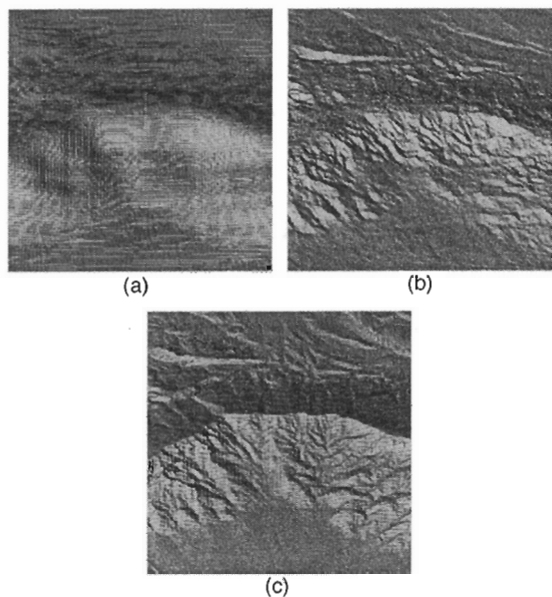


Fig. 13 Three shaded renditions of the Sandia Mountains looking east from above Albuquerque, derived from cubic-interpolated 1-km DEM (a), sharpened 1-km DEM (b), and true 25-m DEM (c).

The ability to accurately register multispectral imagery to a DEM is one factor limiting the accuracy of the elevation sharpening process. For terrain visualization, registration accuracies on the order of those over the present study area appear adequate to generate high-quality shaded renditions from the sharpened data (Fig. 13). Whether the accuracies required for other terrain analysis applications can be achieved using current registration technology is not known.

A more fundamental limitation of the elevation sharpening technique is the extent to which slope and spectral albedo are related. In particular the sharpening technique will not perform well when the surface cover is homogeneous, or when the slope and surface cover are not related at all. Future work will investigate the applicability of our approach for sharpening higher-resolution data.

7 Summary

A new method for enhancing the spatial resolution of a low-resolution DEM using a single higher-resolution multispectral image was described. The method assumes that slope and albedo are related to one another and that functions exist relating the spectral response of a pixel to its underlying gradient components and can be determined empirically. Experimental results over a study area in northern New Mexico containing a diversity of terrain and surface cover are most encouraging.

Currently 30-arcsec topographic data (approximately 1-km resolution) exist over the entire world.¹³ Although much higher-resolution 7.5-arcmin quads are available over the USA, higher-resolution data for other parts of the world are very limited. For applications requiring higher-resolution data over those areas, elevation sharpening provides a cost-effective alternative to interferometric synthetic-aperture radar and to stereo image collection and compilation.

8 Appendix: List of Symbols

i, j	= spatial indices in the x and y (horizontal and vertical) directions
n, n'	= spectral band or index
N	= number of spectral bands
$b(i, j), b(i, j, n)$	= image irradiance (brightness)
p, q	= horizontal and vertical components of the gradient of the elevation surface
$R(p, q)$	= reflectance map
$\rho(i, j)$	= albedo
$\rho(i, j, n)$	= spectral albedo
\mathbf{u}	= reduced dimension spectral (estimator) vector
v	= quantity to be estimated
\tilde{v}	= estimated quantity
$P(\mathbf{u}, v)$	= joint density function
$P(v \mathbf{u})$	= conditional density function
$E(v \mathbf{u})$	= conditional expected value
M	= number of unique estimator vectors (cardinality of \mathbf{u})
m	= index of a particular combination
S_m	= set of pixels in m th combination
N_m	= number of pixels in m th combination
z	= elevation
ϵ	= pixel spacing
z_L, p_L, q_L	= low-resolution elevation and gradients
z_H, p_H, q_H	= high-resolution (estimated) elevation and gradients
f_p, f_q	= lookup tables
t	= iteration index (time)
k, l	= spatial indices relative to pixel i, j
e_H	= horizontal error
z	= true elevation
z^-, z^+	= true minimum and maximum elevation within e_H of center pixel i, j

References

1. B. K. P. Horn, "Height and gradient from shading," *Int. J. Comput. Vis.* 5(1) (1990).
2. K. M. Lee and C. C. J. Kuo, "Shape from shading with a linear triangular element surface model," *IEEE Trans. Pattern. Anal. Mach. Intell.* 15(8), 815-822 (1993).
3. P. S. Tsai and M. Shah, "Shape from shading with variable albedo," *Opt. Eng.* 37(4), 1212-1220 (1998).
4. P. Eliason, L. Soderblom, and P. Chavez, "Extraction of topographic and spectral albedo information from multispectral images," *Photogram. Eng. Remote Sens.* 48(11), 1571-1579 (1981).
5. C. Lee and A. Rosenfeld, "Albedo estimation for scene segmentation," *Pattern Recogn. Lett.* 1, 155-160 (1983).
6. P. S. Tsai and M. Shah, "Shape from shading using linear approximation," *Image Vis. Comput.* 12(8), 487-498 (1994).
7. B. K. P. Horn, "Hill shading and the reflectance map," Presented at Image Understanding Workshop, Palo Alto, CA, 1979.
8. M. J. Carlotto, "A new method for extracting topographic informa-

- tion from a single multispectral image," in *Proc. International Geoscience and Remote Sensing Symp.*, Lincoln NE (1996).
9. K. Ikeuchi, "Constructing a depth map from images," A. I. Memo No. 774, MIT Artificial Intelligence Laboratory (1983).
 10. R. Frankot and R. Chellappa, "Estimation of surface topography from SAR imagery using shape from shading techniques," *Artif. Intel.* **43**, 271-310 (1990).
 11. A. Papoulis, *Probability, Random Variables and Stochastic Processes*, McGraw-Hill (1965).
 12. B. K. P. Horn and M. J. Brooks, "The variational approach to shape from shading," *Comput. Vis. Graph. Image Process.* **33**, 174-208 (1986).
 13. United States Geological Survey, <http://edcwww.cr.usgs.gov/landdaac/gtopo30/> (1999).

Mark J. Carlotto received the BS, MS, and PhD degrees in electrical engineering from Carnegie-Mellon University in 1977, 1979, and

1981, respectively. From 1981 to 1993 he was with The Analytic Sciences Corp. (TASC) in Reading, Massachusetts, involved in a variety of projects in the areas of multispectral image processing, object/change detection, image segmentation, scene analysis, geographical information systems, knowledge-based systems, text processing, and data visualization. Also during this period he was an assistant adjunct professor in the College of Engineering at Boston University where he taught courses in computer architecture and pattern recognition. Dr. Carlotto is now a senior staff scientist with Pacific-Sierra Research Corporation in Arlington, Virginia. His current research interests include automated multispectral image classification, terrain feature extraction, change detection and analysis, and image understanding.